**Electronic Supplementary Information (ESI) for Chemical Communications**

# $ZnIn_2S_4$/g-$C_3N_4$ heterojunction enabled PEC-ECL sensing interface for quenching assay of fipronil

Yao Song[a], Huan Yang[a], Huanyu Cheng[b], Qiumei Feng[a,*] and Po Wang[a,*]

[a] *School of Chemistry and Materials Science, Jiangsu Normal University, Xuzhou 221116, China*

[b] *Department of Engineering Science and Mechanics, Pennsylvania State University, University Park, State College, Pennsylvania 16802, USA*

* Corresponding author.

Phone: +86 516 83403165. Fax: +86 516 83536977.

*E-mail address:* wangpo@jsnu.edu.cn (P. Wang).

## Experimental section

**Materials and Reagents.** N-hydroxysuccinimide (NHS), N-(3-dimethylaminopropyl)-N-ethyl-carbodiimide hydrochloride (EDC), tris (2-carboxyethyl) phosphine hydrochloride (TCEP), chitosan (CS), and (3-aminopropyl) triethoxysilane (APTES) were purchased from Sigma-Aldrich (St. Louis, MO). $KMnO_4$, oleic acid, indium chloride tetrahydrate, thioacetamide, and Zinc chloride ($ZnCl_2$) were purchased from Sinopharm (China). Ascorbic acid (AA) and $K_2S_2O_8$ were supplied by Aladdin Reagent Corporation (Shanghai, China). Carboxylated magnetic beads (20 nm in diameter) were obtained from Xi'an GoldMag Nanobiotech Co., Ltd (Xi'an, China). All other commonly used chemicals were of analytical grade. All experimental procedures involving reagents and nanomaterials strictly adhered to laboratory safety regulations and standard operating protocols. Reagents were stored and handled precisely following the supplier's recommendations. Phosphate buffer solution (PBS; 0.1 M $KH_2PO_4$-$K_2HPO_4$-NaCl; pH 7.4) containing 100 mM $K_2S_2O_8$ as a coreactant was used for ECL detection. All photoelectrochemical (PEC) performance was measured in PBS containing 0.1 mM AA as the electron donor. DNA oligonucleotides used in this work were purchased from Sangon Biological Engineering Technology & Co. Ltd (Shanghai, China), with the sequences listed in Table S1.

**Apparatus.** PEC measurement was carried out on a CHI832A electrochemical workstation (Austin, USA) equipped with a 500 W Xe lamp as the irradiation source.

All ECL signals were recorded on a MPI-A multifunctional electrochemical and chemiluminescent analytical system (Remax Electronic Instrument Limited Co., Xi'an, China, 350–650 nm) and the voltage of the photomultiplier tube (PMT) was set at 700V. The potential scan was from 0 to –1.8 V for signal detection with the scan rate set at 100 mV $s^{-1}$. Electrochemical impedance spectroscopy (EIS) experiments and Mott-Schottky plots were performed on a CHI660C electrochemical workstation (CH Instruments, USA) with the following EIS experimental conditions: DC potential of 0.22 V, frequency range of $10^5$–0.1 Hz; and amplitude of 0.005 V. The experiments were carried out with a three-electrode system: a modified ITO electrode with a diameter of 6 mm as the working electrode, a platinum wire as the counter electrode, and Ag/AgCl as the reference electrode. UV-vis absorption spectra of $ZnIn_2S_4$, g-$C_3N_4$, and $MnO_2$ NFs were obtained on a Shimadzu UV-3600 UV-vis-NIR photospectrometer (Shimadzu Co., Japan) at room temperature. The morphology of g-$C_3N_4$, $ZnIn_2S_4$/g-$C_3N_4$, and $MnO_2$ NFs was characterized by scanning electron microscopy (SEM, JSM-6330F microanalyzer, JEOL, Japan). Transmission electron micrograph (TEM) images of $MnO_2$ NFs and Au NPs were collected from a JSM2100 Plus (JEC, Japan). X-ray photoelectron spectroscopy (XPS) responses of $ZnIn_2S_4$/g-$C_3N_4$ and $MnO_2$ NFs were conducted on a Thermo ESCALAB 250XI instrument with an Al Kα X-ray source. Dynamic light scattering (DLS) measurement of $MnO_2$ NFs was performed by a BI-200 SM light scattering apparatus (Brookhaven Instruments Co., USA) equipped with a digital correlator at 640 nm. Fourier transform infrared (FT-IR) spectra of g-$C_3N_4$, $ZnIn_2S_4$, $ZnIn_2S_4$/g-$C_3N_4$ and $MnO_2$ NFs were recorded on

an AVATAR-370 Fourier transform infrared spectrometer (Thermo Nicolet, USA). Fluorescence spectra of FAM-labelled nucleic acid were recorded on an RF-5301PC fluorescence spectrometer (Shimadzu Co., Japan).

**Synthesis of $ZnIn_2S_4$/g-$C_3N_4$.** $ZnIn_2S_4$/g-$C_3N_4$ composites were obtained via a two-step fabrication process. g-$C_3N_4$ nanosheets was first prepared according to the reported method.[S1] In detail, 10 g urea underwent calcination (550°C, 4 h, 5°C/min heating rate) in a closed ceramic crucible. The obtained yellow blocky g-$C_3N_4$ materials were ground into powder. Afterward, the bulk product underwent calcination again in an open ceramic crucible. The obtained powers were purified via three deionized water and 60°C drying to produce g-$C_3N_4$ nanosheets. To synthesize $ZnIn_2S_4$, 0.225 g thioacetamide, 0.293 g indium chloride tetrahydrate, and 0.068 g zinc chloride were dissolved in 30 mL of deionized water and then stirred for 40 min. Subsequently, 0.2 g g-$C_3N_4$ nanosheets from the first step were dissolved in the above mixture, followed by stirring for 40 min. Next, the mixed products were placed in a stainless Teflon-lined autoclave and kept for 1 h at 160 °C. After washing with ethanol and deionized water, the collected precipitate was dried in a 60 °C vacuum oven to obtain 0.35 g $ZnIn_2S_4$/g-$C_3N_4$. As a control, $ZnIn_2S_4$ was fabricated using the same procedure without the addition of g-$C_3N_4$ nanosheets.

**Preparation of H4-$MnO_2$.** The preparation of H4-$MnO_2$ involved the synthesis of $MnO_2$ NFs and the subsequent modification at the 3′ end of H4. Firstly, oleic acid was used as the reducing agent to reduce $KMnO_4$. 0.5 g $KMnO_4$ was added in 250 mL of ultrapure water, followed by stirring at room temperature for 30 min. Subsequently, 5

mL of oleic acid was slowly injected into the above solution to form a stable emulsion. Following a 4 h reaction at 25°C, the resultant mixture was centrifuged (8000 rpm, 10 min) and dried to isolate 0.25 g brown-black $MnO_2$ NFs. To further form amino-functionalized $MnO_2$ NFs, 1 mL of 3-aminopropyltriethoxysilane (10% v/v, prepared in ethanol) was added in 0.25 g $MnO_2$ NFs. Under a nitrogen atmosphere, the reaction solution was vigorously stirred for 6 h at 120 °C. Followed by rinsing with ethanol and water, amino groups-assembled $MnO_2$ NFs were resuspensed in 2 mL of PBS. To prepare H4-$MnO_2$, 200 μL of 20 μM H4 was injected into the above prepared 800 μL of $MnO_2$ NFs and stirred at 25 °C for 24 h. Before use, carboxyl groups-modified H4 strands were activated with a mixed N-(3-dimethylaminopropyl)-N-ethyl-carbodiimide hydrochloride (EDC, 20 mg/mL) and N-hydroxysuccinimide (NHS, 10 mg/mL) for 1 h at 25 °C. After centrifuging and washing with PBS twice, H4-$MnO_2$ was generated via amide bond and subsequently resuspended in 1 mL of PBS for subsequent usage.

**Release of fipronil-dependent M strands.** Magnetic bead separation combining with aptamer recognition was performed to transduce the signal from fipronil to nucleic acid chain. As Scheme 1A showing, 800 μL of 1 mg/mL carboxyl-modified magnetic beads were activated by the same steps as those for H4 strands. After that, 200 μL of 20 μM amino-modified fipronil aptamer was injected into the activated magnetic beads. Under gentle shaking, the reaction mixture was incubated at 37 °C for 6 h to form aptamer-coated magnetic beads bioconjugates (aptamer/magnetic beads). Followed by magnetic separation and washing, aptamer/magnetic beads were

added into 200 μL of 20 μM M strands, followed by incubating for 1 h to achieve aptamer:M duplex-modified magnetic beads. After washing, these bioconjugates were further reacted with different concentrations of fipronil for 1 h. Finally, fipronil-dependent M strands were released into the supernatant after removing the sediment by magnetic separation, realizing signal transduction.

**Preparation of P strands.** The upstream CHA I was carried out as the first-step signal amplification, with the corresponding process shown in Scheme 1B. In detail, 100 μL of 20 μM H1 strands were mixed with the releasing M strands and incubated for 40 min. Meanwhile, 20 μM H2 and 2 mM $Mn^{2+}$ were mixed together and reacted for 50 min at 37 °C to drive CHA I, releasing the intermediate S strands into the solution under the cleavage process of $Mn^{2+}$-specific DNAzyme.

**Fabrication of the dual-mode biosensor.** As Scheme 1C illustrating, 10 μL of 0.8 wt% chitosan (CS) and 10 μL of $ZnIn_2S_4$/g-$C_3N_4$ were mixed and then dropped on the working area of indium tin oxide (ITO), followed by drying at 25 °C for the immobilization of $ZnIn_2S_4$/g-$C_3N_4$. Next, the functionalized electrode was soaked in 20 mM PBS (pH=7.4) for 1 h to remove loose $ZnIn_2S_4$/g-$C_3N_4$. The obtained $ZnIn_2S_4$/g-$C_3N_4$/ITO was incubated in 500 μL of 2.5 μM carboxyl groups-modified H3 strands, which were further activated by the same steps as those for H4 strands. Thereafter, H3/$ZnIn_2S_4$/g-$C_3N_4$/ITO was further incubated with 200 μL of mixture containing the as-prepared P strands and H4-$MnO_2$. The downstream CHA II on the electrode surface was completed for 60 min at 37 °C. Ultimately, PEC and ECL signals from the fabricated biosensor were recorded in 0.1 mM AA and 100 mM

$K_2S_2O_8$, respectively. After each modification, the electrode surface was washed with PBS.

**Sample preparation.** Given fipronil exposure in food field, lettuce leaves and eggs provided by the local market were chosen to evaluate the practicability of the biosensor. According to the reported method,[S2] lettuce leaves and eggs were spiked with 1 nM fipronil. Followed by reaction at 25 °C for 30 min, lettuce leaves were added in a mixed acetonitrile and ultrapure water solution (20 mL, 3:1) and then sonicated for 30 min. After centrifuging (5000 rpm, 5 min), the collected supernatant underwent 0.22 μM membrane filtration and then treated with rotary evaporation at 65 °C, resulting in the concentrated fipronil. Concurrently, 1 mL of homogenized, fipronil-spiked eggs ground with a mixer was transferred to centrifuge tubes. Subsequently, the extraction was treated by adding 10 mL of acetonitrile, 4 g of anhydrous $MgSO_4$, and 2 g of anhydrous NaCl to the centrifuge tube, followed by vigorous shaking for 30 min. After that, the extraction of fipronil from lettuce leaves followed the same process as that from eggs. Lastly, the dual-mode biosensor was reacted with these concentrated fipronil samples using the detection process described above. Also, gas chromatography tandem mass spectrometry (GC-MS) was employed as a control standard method for parallel sample test to validate the sensing precision.

**Supplementary Figures**

A collection of band spectra was characterized for the optical properties and band structures of the heterojunction. As illustrated in Fig. S1A, g-$C_3N_4$ and $ZnIn_2S_4$ exhibited absorption edges at about 400 nm and 390 nm, respectively. Via the

classical Tauc plots method, the band gap energies ($E_g$) of g-$C_3N_4$ and $ZnIn_2S_4$ were 2.81 eV and 2.62 eV, respectively (Fig. S1B). Furthermore, the XPS valence band (VB) spectra showed that the VB positions of g-$C_3N_4$ and $ZnIn_2S_4$ were 1.67 eV and 2.00 eV (Fig. S1C), calculated from the formula $E_{NHE}$(the normal hydrogen electrode)=$E_{VB}$+$E_{wf}$(4.2 eV)–4.44. According to the Mott-Schottky band potential, the conduction band (CB) positions of g-$C_3N_4$ and $ZnIn_2S_4$ were determined to be –1.11 eV (Fig. S1D) and –0.62 eV (Fig. S1E) from the equation $E_{NHE}$=$E_{VB}$+$E_{SCE}$+0.24. The results of Fig. S1C-E combined with the formula $E_{VB}$=$E_g$+$E_{CB}$ further revealed the calculated $E_g$ values of 2.78 eV and 2.68 eV for g-$C_3N_4$ and $ZnIn_2S_4$, which were highly consistent with the results in Fig. S1B. In addition, the band structure alignments for g-$C_3N_4$ and $ZnIn_2S_4$ (Fig. S1F) revealed the precondition of Z-scheme charge transfer for $ZnIn_2S_4$/g-$C_3N_4$ heterojunction.

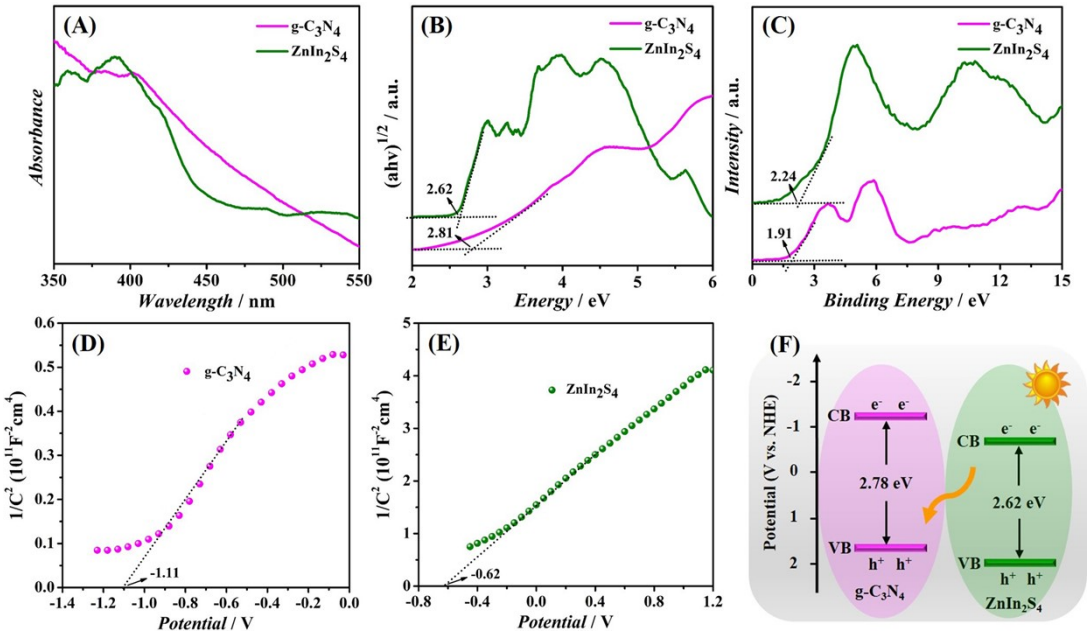


**Fig. S1** (A) UV-vis diffuse reflection spectra of g-$C_3N_4$ and $ZnIn_2S_4$. (B) Band gap energies of g-$C_3N_4$ and $ZnIn_2S_4$ obtained from the transformational Tauc plots with

the Kubelka-Munk function. (C) VB XPS spectra of g-$C_3N_4$ and $ZnIn_2S_4$. Mott-Schottky plots of g-$C_3N_4$ (D) and $ZnIn_2S$ (E). (F) Schematic diagram of band structure level of g-$C_3N_4$ and $ZnIn_2S_4$.

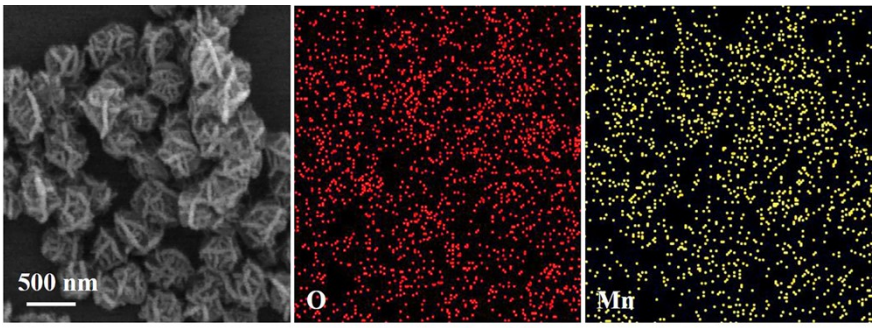


**Fig. S2** SEM image and the corresponding EDS elemental mapping images of O and Mn in $MnO_2$ NFs.

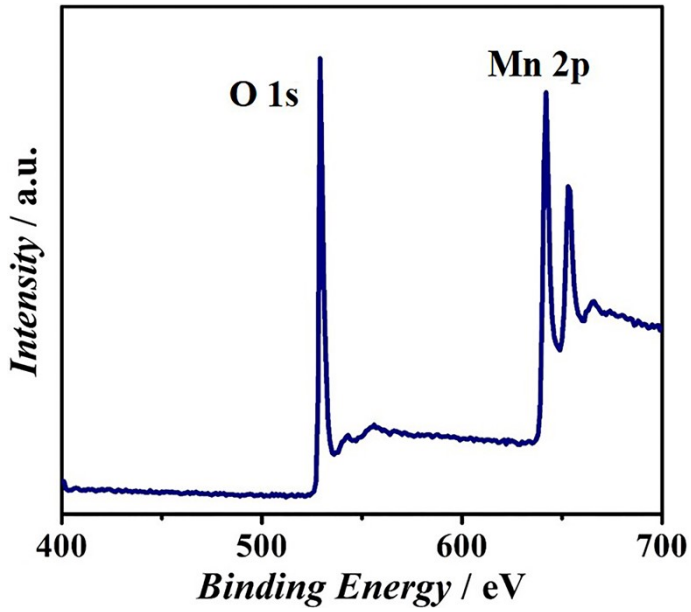


**Fig. S3** A wide range XPS spectra of $MnO_2$ NFs.

To ensure the feasibility of the signal transduction from fipronil to M strands and double-step CHA, UV-vis absorption and fluorescence emission were performed. As illustrated in Fig. S4A, 2.5 μM aptamer displayed an obvious absorption peak at 268 nm (curve a). Followed by incubating with magnetic beads and magnetic separation, the absorption peak of the supernatant was evidently reduced (curve b), revealing the

successful assembly of aptamer on the surface of magnetic beads. Similarly, compared with that of 2.5 μM M (curve c), the supernatant of aptamer/magnetic beads treating with M exhibited a very lower absorption peak (curve d), attributing to the formation of aptamer:M duplex-modified magnetic beads. When the above compound was further reacted with target fipronil and magnetic separation, a clear peak intensity of the supernatant was observed in curve e, revealing the special recognition of aptamer to fipronil and then the signal transduction of fipronil to M strands.

By virtue of fluorescence resonance energy transfer (FRET) between gold nanoparticle (Au NP) and carboxyfluorescein (FAM), fluorescence measurement was performed to test the feasibility of upstream CHA I. As expressed in Fig. S4B, FAM and Au NP were modified at the 5′ end and 3′ end of H1 strands, respectively. The used Au NP possessed spherical structure (Fig. S5). In Fig. S6, the average diameter of Au NPs was about 7 nm through the determination of dynamic light scattering. After the modification with H1 strands, the size of H1-Au NPs increased to 9 nm. Meanwhile, zeta potential analysis in Fig. S7 revealed that the obtained H1-Au NPs (-23.1 mV) showed a more negative charge than that of Au NPs (-14.9 mV). Thus, the above results indicated the successful preparation of H1-Au NPs. Due to the hairpin structure of H1, the fluorescence intensity of FAM could be quenched by Au NP at a close distance (curve a). When meeting the fipronil-dependent M strands, the hairpin structure of Au-H1-FAM transitioned into a rod-like conformation via hybridization with M strands. The increased separation between Au NP and FAM led to partial recovery of FAM fluorescence (curve b). Upon the addition of H2 and $Mn^{2+}$ into Au-

H1-FAM:M compound and then centrifugation (curve c), the supernatant showed a stronger fluorescence intensity than that of Au-H1-FAM:M compound. The cleavage of $Mn^{2+}$-specific DNAzyme completely separated FAM from Au NP, yielding a total recovery of FAM fluorescence. Therefore, the above fluorescence changes demonstrated the viability of CHA I with the help of $Mn^{2+}$-specific DNAzyme.

In order to verify the stepwise construction process of the downstream CHA II on the electrode surface, UV-vis absorption and fluorescence measurements were both carried out in Fig. S4C-D. In contrast to 2.5 μM H3 (Fig. S4C, curve a), the remaining solution of H3 after incubating with $ZnIn_2S_4$/g-$C_3N_4$/ITO exhibited a very low absorption peak (Fig. S4C, curve b), indicating the successful introduction of H3 to the electrode interface. When H3/$ZnIn_2S_4$/g-$C_3N_4$/ITO was reacted with P (Fig. S4C, curve d) or FAM-labelled P (P-FAM, Fig. S4D, curve b), UV-vis absorption peak and fluorescence signal were both reduced compared with those of the original P (Fig. S4C, curve c) or P-FAM (Fig. S4D, curve a). However, after the further incubation with H4 strands, there were both clear UV-vis absorption (Fig. S4C, curve e) and fluorescence signal (Fig. S4D, curve c) for the reaction solution, attributing to the release of P or P-FAM strands. Thus, the above results confirmed that the release of P strands from the upstream CHA I could effectively trigger the downstream CHA II.

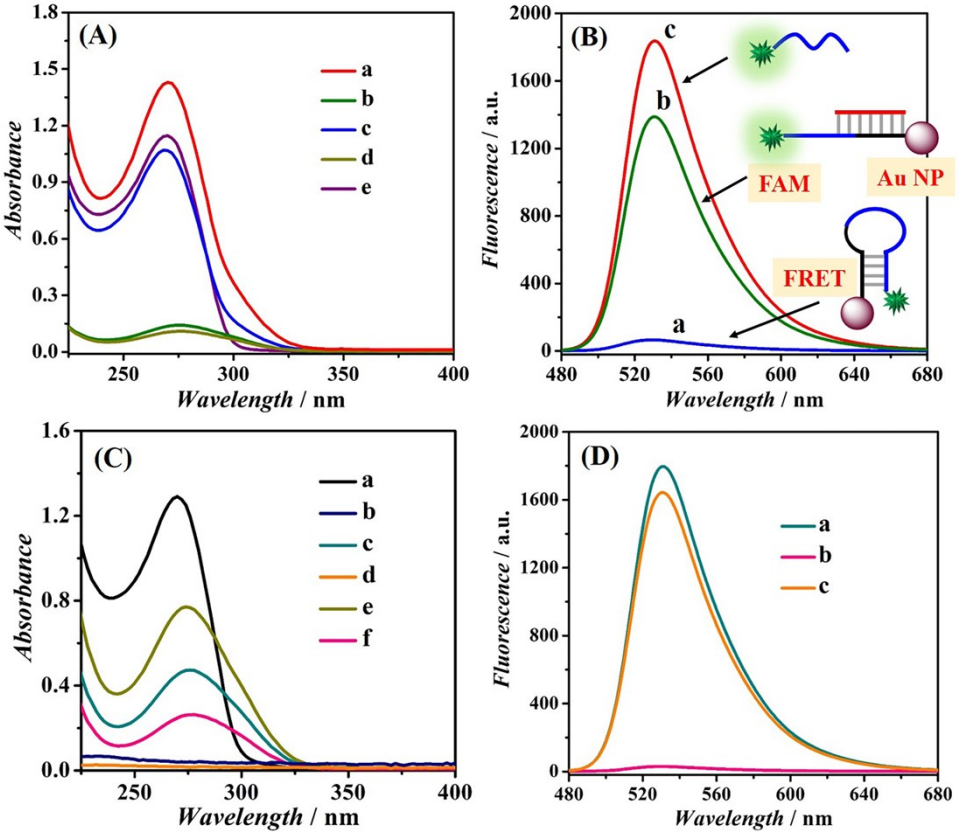


**Fig. S4** (A) UV–vis absorption spectra for the signal transduction of fipronil to M strands: (a) 2.5 μM aptamer, (b) the supernatant of magnetic beads + aptamer, (c) 2.5 μM M, (d) the supernatant of magnetic beads + aptamer + M, (e) the supernatant of d further incubated with fipronil. (B) Fluorescence spectra of upstream CHA I relying on FRET between FAM and Au NP: (a) Au NP + H1-FAM, (b) Au-H1-FAM + M, (c) the supernatant of b incubating with the mixture of H2 and $Mn^{2+}$ after centrifugation. (C) UV–vis absorption spectra for downstream CHA II: (a) 2.5 μM H3, (b) H3 after incubating with $ZnIn_2S_4$/g-$C_3N_4$/ITO, (c) 2.5 μM P, (d) P after incubating with H3/$ZnIn_2S_4$/g-$C_3N_4$/ITO, (e) 2.5 μM H4, (f) H4 after incubating with P/H3/$ZnIn_2S_4$/g-$C_3N_4$/ITO. (D) Fluorescence spectra of downstream CHA II: (a) 2.5 μM P-FAM, (b) P-FAM after incubating with H3/$ZnIn_2S_4$/g-$C_3N_4$/ITO, (c) the supernatant of P-FAM/H3/$ZnIn_2S_4$/g-$C_3N_4$/ITO incubating with H4.

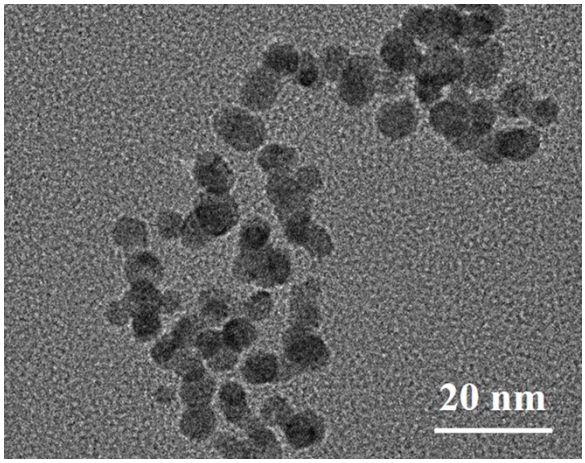


**Fig. S5** TEM image of Au NPs.

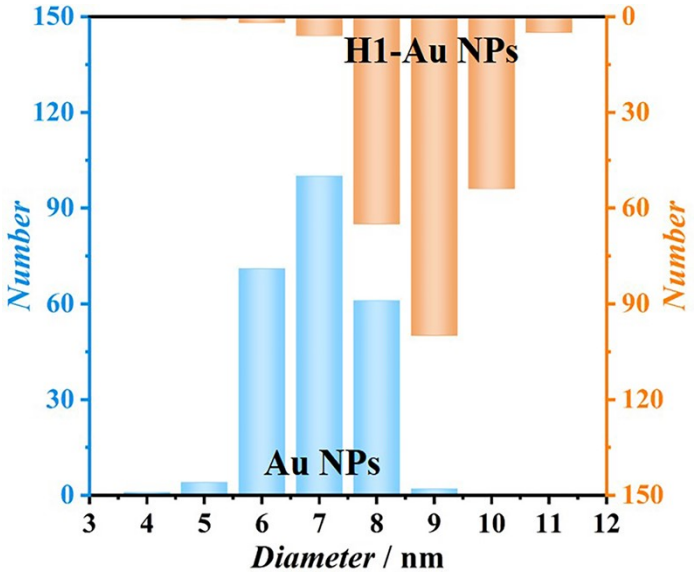


**Fig. S6** Hydrodynamic sizes of Au NPs measured by dynamic light scattering.

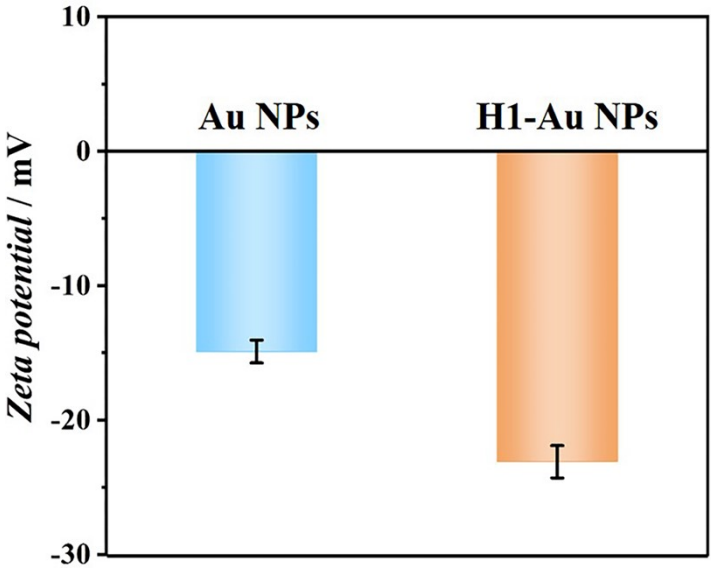


**Fig. S7** zeta potentials of Au NPs and H1-Au NPs.

To learn the electrode interface properties, cyclic voltammetry (CV) and electrochemical impedance spectrum (EIS) tests were conducted in a $[Fe(CN)_6]^{3-/4-}$ solution. As illustrated in Fig. S8A and S8B, in contrast to bare ITO (curve a), $ZnIn_2S_4$/g-$C_3N_4$/ITO displayed a reduced current response and enhanced peak separation ($\Delta E_p$) in CV, as well as an increased interfacial charge-transfer resistance ($R_{et}$) in EIS, attributing to the low conductivity of the mixed CS and $ZnIn_2S_4$/g-$C_3N_4$. Subsequently, H3 (curve c), the releasing P strands from CHA I (curve d), and H4-$MnO_2$ (curve e) were introduced step by step, resulting in the continuous reduction in peak current and rise in $\Delta E_p$ for CV responses, as well as unrelenting enhancement in $R_{et}$ for EIS signals. These phenomena verified that the self-assembled, negatively charged nucleic acid chains hindered $[Fe(CN)_6]^{3-/4-}$ diffusion to the electrode surface due to the electrostatic repulsions and the sensing interface was successfully fabricated as expected.

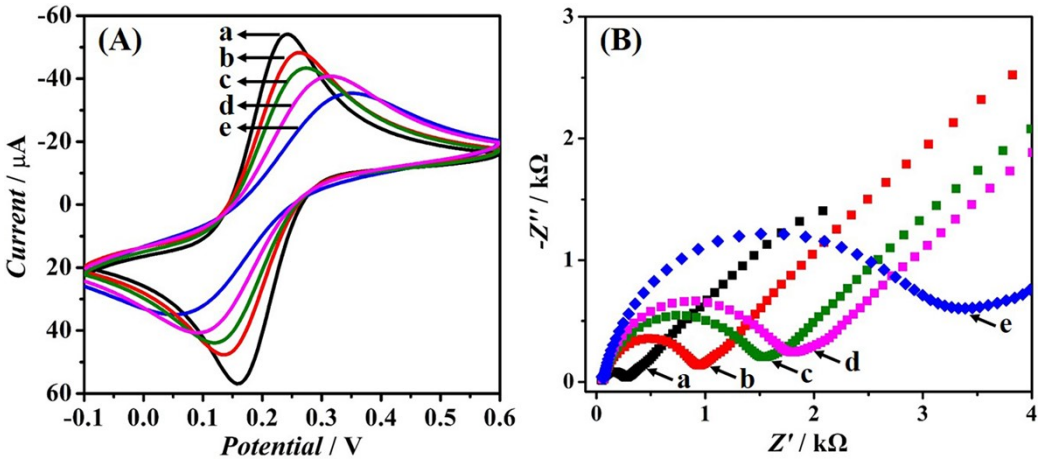


**Fig. S8** CV curves (A) and EIS plots (B) of different modified electrodes: (a) bare ITO, (b) $ZnIn_2S_4$/g-$C_3N_4$/ITO, (c) H3/$ZnIn_2S_4$/g-$C_3N_4$/ITO, P/H3/$ZnIn_2S_4$/g-$C_3N_4$/ITO (d) before and (e) after incubating with H4-$MnO_2$.

Since $ZnIn_2S_4$/g-$C_3N_4$ was fixed onto the electrode surface through the adhesive property of CS, the weight percent (wt%) of CS was optimized (Fig. S9). As seen, the photocurrent and ECL intensities gradually enhanced with the increase of CS wt% from 0.2 to 0.8. The increased CS concentration would prevent $ZnIn_2S_4$/g-$C_3N_4$ from falling off the electrode surface. However, when the wt% exceeded 0.8, photocurrent and ECL signals both reduced, attributing to non-conductive property of CS.

The pH influence of the electrolyte on ECL response was investigated in Fig. S10. With an increasing pH from pH 5 to 10, the ECL intensity of biosensor gradually increased for the pH 5 to 8 and then decreased with the further increasing pH value. The enhancement in ECL emission was mainly due to the adsorption of lewis bases, which changed the surface states of nanomaterials.[S3] This phenomenon was consistent with previous result.[S4] Finally, pH 7.4 PBS containing 100 mM $K_2S_2O_8$ was chosen for ECL detection.

Besides, the reaction times of CHA I and CHA II were also optimized in Fig. S11 and S12, respectively. The increased incubation time (10 to 50 min for CHA I and 10 to 60 min for CHA II) continuously decreased photocurrent and ECL signals before reaching a plateau. These results indicated that the reaction times of 50 min and 60 min were sufficient to separately execute CHA I and CHA II. Thus, 0.8 wt% CS, 50 min of reaction time for CHA I, and 60 min of incubation time for CHA II were chosen in subsequent experiments unless specified otherwise.

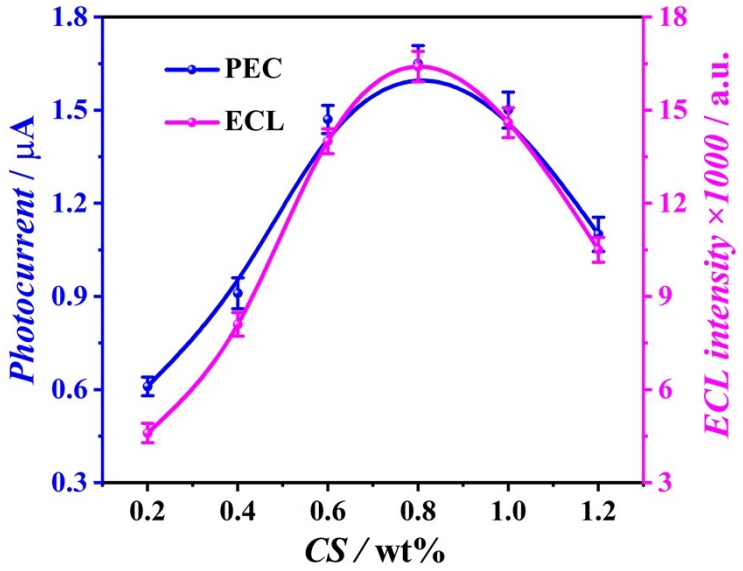


**Fig. S9** Photocurrent response and ECL intensity of $ZnIn_2S_4$/g-$C_3N_4$/ITO as a function of the CS concentration.

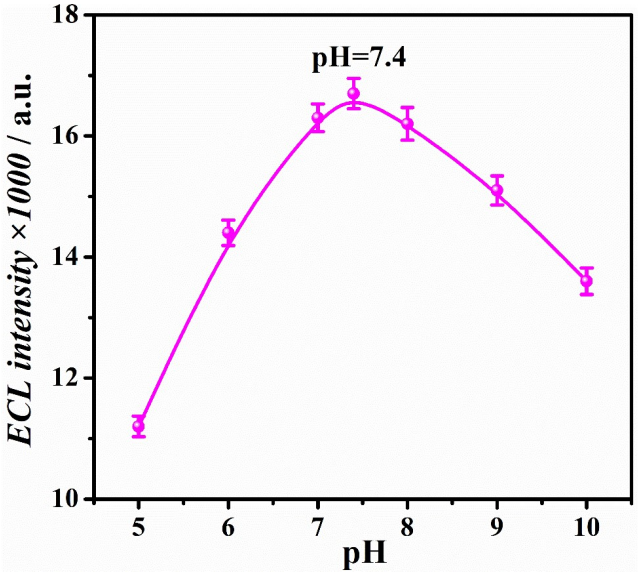


**Fig. S10** Effect of pH value for the electrolyte on the ECL response of $ZnIn_2S_4$/g-$C_3N_4$ heterojunction modified electrode.

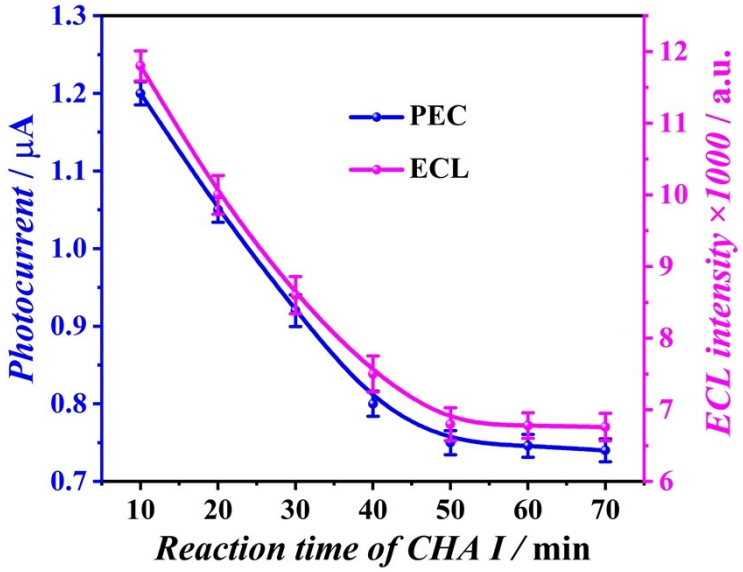


**Fig. S11** Effect of CHA I reaction time on photocurrent response and ECL intensity of the sensing system. The concentration of fipronil was 50 pM.

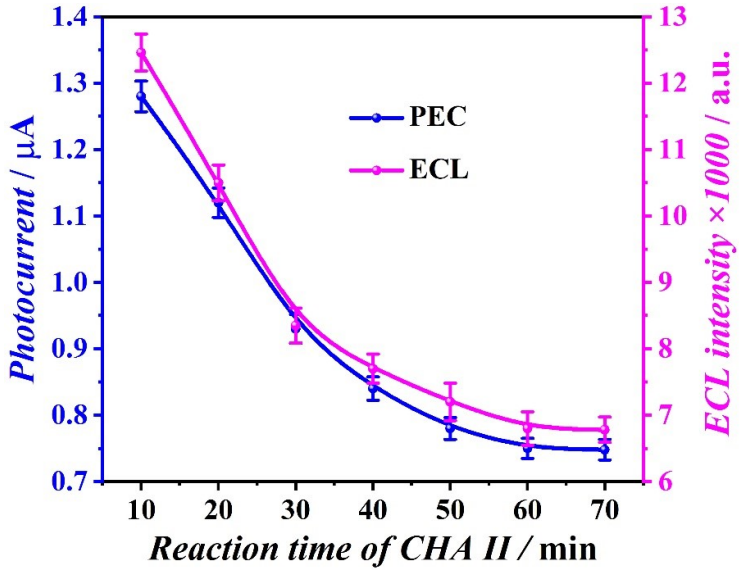


**Fig. S12** The dependence of photocurrent response and ECL intensity on the reaction time of CHA II on the sensing interface. The concentration of fipronil was 50 pM.

The detection and storage stabilities of PEC and ECL responses on the sensing interface was evaluated in Fig. S13-S15. It could be seen that both photocurrent (Fig. S13) and ECL intensities (Fig. S14) remained nearly unchanged with the relative standard deviation (RSD) of less than 5%, illustrating good stability of the dual-mode sensing. Moreover, the long-term storage stability was explored by continuous detection with the same sensing interface, which was stored at 4 °C in the dark when not in use. PEC and ECL measurements were performed for 14 days at 2-day intervals. As displayed in Fig. S15, no obvious change was observed within14 days, indicating that the as-prepared dual-mode biosensor exhibited excellent storage stability. The reproducibility was evaluated using six independently fabricated electrodes under identical experimental conditions. 4.5% of RSD for photocurrent and 4.8% of RSD for ECL signal were obtained, implying an acceptable precision of the proposed system.

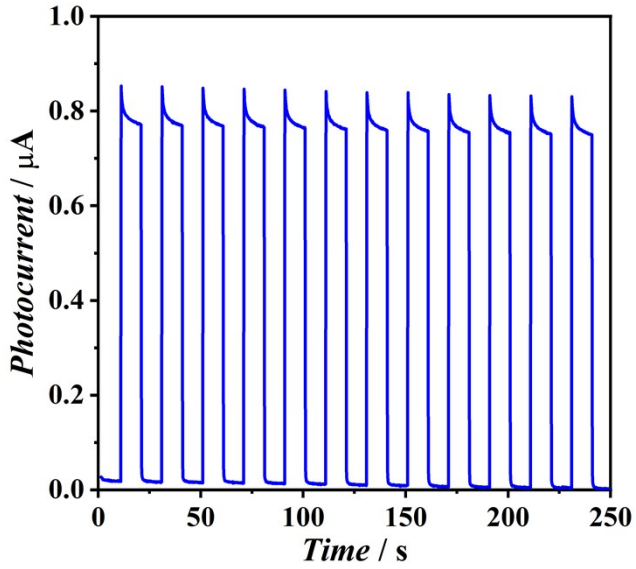


**Fig. S13** Time-based photocurrent responses of the biosensor with light on and off.

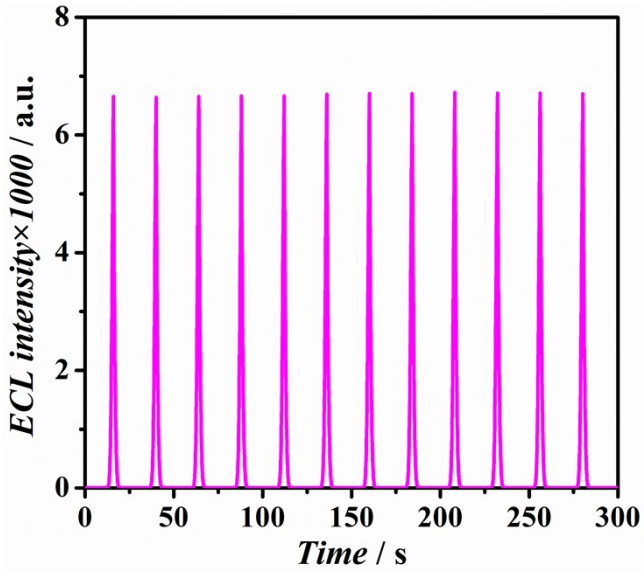


**Fig. S14** ECL emission stability of the proposed sensing system under continuous cyclic potential scans for 12 cycles.

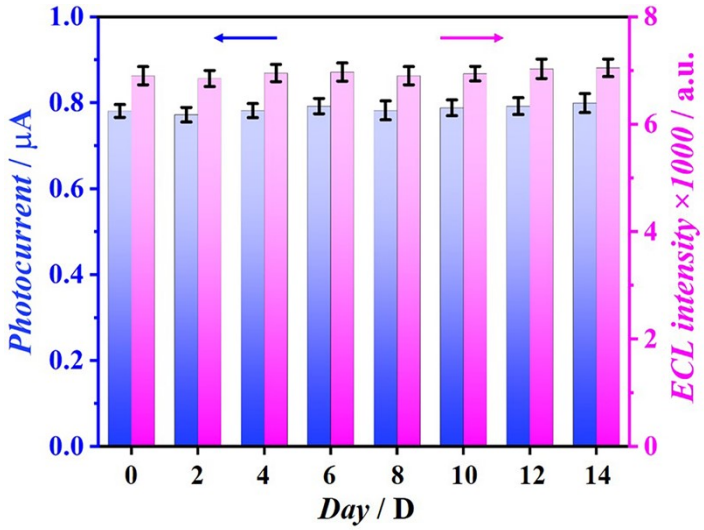


**Fig. S15** Bar graph of the long-term storage stability of the PEC-ECL biosensor (0-14 days).

**Table S1.** DNA sequences used in this work.

| Name | Sequences (5′ to 3′) |
|---|---|
| Aptamer | $NH_2$-TGTACCGTCTGAGCGATTCGTACAGTTTCTGGAGGACTGGGCGGGGTGACGGTTATGAGCCAGTCAGTGTTAAGGAGTGC |
| M | AGCATCGTCACCCCGCCCAGTCCTCCAGAA |
| H1 | TTCTGGAGGACTGGGCGGGGTGACGATGCTGrACGCATGCAAAGCCGCCCAGTCC |
| H2 | AACCTTTGCATGCGCGAGCCGGACGACAGCATCGACACCCCGCCC |
| H3 | COOH-GGACTGGGCGGCTTTGCATGCGTCCATGTGTAGACGACAGCCGCCCACTTGAC |
| H4 | GGACGCATGCAAAGCCGCAGCATCTAACCTTCTGCACGGTTTGCATGCATGTG-COOH |

**Table S2.** Comparison between this work and other fipronil detection methods.

| Methods | Detection limit | Liner range | Ref. |
|---|---|---|---|
| Surface-enhanced Raman scattering | 9.9 nM | $10^{-5}$ M – $10^{-9}$ M | S5 |
| Surface-enhanced Raman scattering | 15.68 nM | 50 nM − 400 nM | S6 |
| Electrochemical | 76 pg/mL | 100 pg/ mL − 100 μg/mL | S7 |
| Fluorescence | 0.046 ng/mL | 0.05 ng/mL – 10 ng/mL | S8 |
| Fluorescence | 9.30 nM | $1\times10^{4}$ nM – $9\times10^{4}$ nM | S9 |
| Colorimetric | 3.89 μM | 40 – 300 μM | S10 |
| Fluorescence | 4.4 nM | 0–0.15 mM | S11 |
| Enzyme linked immunosorbent assays | 0.2 ng/mL | 10 ng/mL – 30 ng/mL | S12 |
| PEC-ECL | 6.8 fM (PEC) 6.2 fM (ECL) | $2\times10^{-14}$ M – $1\times10^{-8}$ M | This work |

## References


[S1] X. Bao, M. Liu, Z. Wang, D. Dai, P. Wang, H. Cheng, Y. Liu, Z. Zheng, Y. Dai and B. Huang, *ACS Catal.*, 2022, **12**, 1919–1929.

[S2] X. Zhang, Y. Zhou, X. Huang, X. Hu, X. Huang, L. Yin, Q. Huang, Y. Wen, B. Li, J. Shi and X. Zou, *Food Chem.*, 2023, **407**, 135115.

[S3] G. Zou and H. Ju, *Anal. Chem.*, 2004, **76**, 6871–6876.

[S4] L. Zhao, X. Song, Y. Li, H. Jia, N. Zhang, Q. Wei, D. Wu and H. Ju, *Biosens. Bioelectron.*, 2023, **221**, 114925.

[S5] N. R. Barveen, S. Chinnapaiyan, C. Zeng, C. Huang, Y. Lin and Y. Cheng, *J. Hazard. Mater.*, 2024, **480**, 135907.

[S6] Y. Zhang, X. Bai, W. Chen, Y. Fan, Y. Tang and G. Huang, *J. Food Meas. Charact.*, 2024, **18**, 9846–9855.

[S7] B. Jia, B. He, R. Liu, J. Yang, W. Ren, Z. Suo and Y. Xu, *Food Chem.*, 2025, **470**, 142662.

[S8] X. Lai, W. Cao, G. Zhang, E. H. Ang, L. Su, C. Liu, W. He, W. Lai and S. Deng, *Chem. Eng. J.*, 2024, **501**, 157565.

[S9] A. S. Gangadharan, D. T. Thangadurai, K. Senthilkumar, V. M. Vasanthakannan, N. Manjubaashini, D. Nataraj and N. K. Kalagatur, *ACS Appl. Nano Mater.*, 2024. **7**, 21388–21400.

[S10] J. Ge, L. Wang, X. Pan, C. Zhang, M. Wu and S. Feng, *Analyst*, 2023, **148**, 5395–5401.

[S11] X. Liu, J. Song, X. Zhang, S. Huang, B. Zhao and X. Feng, *Food Chem.*, 2023, **413**, 135639.

[S12] K. Wang, N. Vasylieva, D. Wan, D. A. Eads, J. Yang, T. Tretten, B. Barnych, J. Li, Q. Li, S. Gee, B. D. Hammock and T. Xu, *Anal. Chem.*, 2019, **91**, 1532–1540.